Scientific Research Publishing

Three-Temperature Model Applied to Thermochemical Non-Equilibrium Reentry Flows in 2D—Seven Species

Edisson Sávio de Góes Maciel

Department of Mathematics, University of Pernambuco, Recife, Brazil
Email: esgm@poli.br

Abstract

In this work, a study involving the fully coupled Euler and Navier-Stokes reactive equations is performed. These equations, in conservative and finite volume contexts, employing structured spatial discretization, on a condition of thermochemical non-equilibrium, are analyzed. High-order studies are accomplished using the Spectral method of Streett, Zang, and Hussaini. The high enthalpy hypersonic flows around a circumference, around a reentry capsule, along a blunt body, and along a double ellipse in two-dimensions are simulated. The Van Leer, Liou and Steffen Jr., and Steger and Warming flux vector splitting algorithms are applied to execute the numerical experiments. Three temperatures, which are the translational-rotational temperature, the vibrational temperature, and the electron temperature, are used to accomplish the numerical comparisons. Excellent results were obtained with minimum errors inferior to 6.0%. The key contribution of this work is the correct implementation of a three temperature model coupled with the implementation of three algorithms to perform the numerical simulations, as well the description of energy exchange mechanisms to perform more realistic simulations.

1. Introduction

Several conceptual designs for vehicles that would fly in the atmosphere at hypersonic speeds have been developed recently [1]. For typical flight conditions, the air that envelops these vehicles is chemically reacted, vibrationally excited, and ionized. These reactions and excitation processes occur at rates similar to the

rate of fluid motion, which results in a state of thermochemical non-equilibrium. The thermochemical state of the gas influences its dynamics and affects the aerodynamic forces and heat transfer acting on the vehicle.

The motivation for multi-temperature model studies often originates for ionized flows owing to the wide disparities in the masses of the constituent species [2]. In this regard, the accuracy of macroscopic temperature models, such as the Landau-Teller translation-vibration (T-V) model, can lead to questioning of the underlying approximations. Such questioning in the past invariably has lead to the development of gas kinetic schemes, such as the Bhatnagar-Gross-Krook scheme [3], to describe the energy exchanges. In addition, the extended Navier-Stokes equations [4] are often used for high-altitude hypersonic flows to accurately capture the shock and provide more information than the classical Navier-Stokes equations can provide. However, the subjective question of the effect of the various energy exchanges using approximate macroscopic temperature models on the shock structure of hypersonic flows can be answered with greater ease if the analysis is made for flows within the continuum regime.

Spectral methods are considered a class of solution techniques using sets of known functions to solve differential equations [5]. Such methods are generally considered high order and capable of obtaining solutions with a high resolution. Unlike finite-difference and finite-element methods, spectral methods utilize an expansion in terms of global, rather than local, basis functions to represent the solution of a differential equation. When properly applied, these techniques accurately resolve phenomena on the scale of the mesh spacing. The order of truncation error decay with mesh refinement is also higher than which can be achieved with finite-difference and finite-element methods. For problems with smooth solutions, it is possible to produce spectral method whose truncation error goes to zero as faster than any finite power of the mesh spacing (exponential convergence).

In this work, a study involving the fully coupled Euler and Navier-Stokes reactive equations is performed. These equations, in conservative and finite volume contexts, employing structured spatial discretization, on a condition of thermochemical non-equilibrium, are analyzed. High-order studies are accomplished using the spectral method of [6]. The high enthalpy hypersonic flows around a circumference, around a reentry capsule, around a blunt body, and around a double ellipse in two-dimensions are simulated. The [7] [8] [9] flux vector splitting algorithms are applied to execute the numerical experiments. The Euler backward integration method is employed to march the schemes in time. The convergence process is accelerated to steady state condition through a spatially variable time step procedure, which has proved effective gains in terms of computational acceleration (see [10] [11]). The reactive simulations involve Earth atmosphere chemical model of seven species and eighteen reactions, based on the [12] model. Three temperatures, which are the translational-rotational temperature, the vibrational temperature, and the electron temperature, are used to accomplish the numerical comparisons. Excellent results were obtained with minimum errors inferior to 6.0%. Moreover, the implementation of a three tempera-

ture model has a great impact to the CFD community in terms of numerical tools available to study thermochemical non-equilibrium flows in two-dimensions more realistically.

The main contribution and originality of this paper is concerned with the three-temperature model studied in it. As [21] has explained, the use of a three temperature model is more appropriated to describe the flow field in the case of numerical simulations of fluid dynamics. The translational and vibrational temperatures, case of two temperature models, are not sufficient to highlight the main features of the flowfield and the use of a third temperature, the electron temperature, is fundamental to describe more correctly the flow physics for the cases of weakly ionization, as is the case. On the other hand, this paper also incorporates the implementation of three upwind numerical algorithms on a context of finite volumes discretization and reactive equations and describes them with details. Although the numerical algorithms were not new for the CFD community, their implementations for such discretization and for reactive formulation is also a original contribution of this work. Moreover, the description of the most important energy exchanges between molecules and atoms, as well electrons, are also pointed out as key mechanisms to be considered in a more realistic scenario of fluid flow. The key contribution of this work is the correct implementation of a three-temperature model coupled with the implementation of three algorithms to perform the numerical simulations, as well the description of energy exchange mechanisms to perform more realistic simulations.

Small number of papers related to the three-temperature and multi-temperature models is available in the CFD literature. With it in mind, this paper aims to fill this space and to provide efficient tools to perform such numerical simulations. For example, the majority of papers lead to one- and two-temperature models and with a minor number of exchange mechanisms to describe the energy change between atoms, molecules, and electrons. The three-temperature model is more involved with the physics and chemistry of the reactive Euler and Navier-Stokes equations, obtaining better results than the one- and two-temperature counterparts. Moreover, the three algorithms studied in this paper have description for perfect gas formulation, being rare the implementation to models of one- and two-temperatures. The present manuscript is an original and detailed description of their implementations for reactive gas flow. The use of a spectral method for the reactive Euler and Navier-Stokes equations is also the extension of the perfect gas formulation to a reactive gas flow one. All of these requisites point out to the original contribution of this work to the CFD state-of-art in terms of non-equilibrium thermal and chemical modeling and reentry flows.

2. Spectral Method

On this current work, a spectral method is applied to assure that high order solutions are obtained by the numerical algorithms. Two classes of techniques for spectral discretization are referred to as tau and collocation methods [6] [13]. The latter technique is used here. In this scheme, the approximation series is de-

termined by satisfying the differential equation exactly at a set of distinct collocation points. The locations of these points in the domain are linked to the choice of basis function. In this study, arbitrary collocation points are implemented. The collocation method is used here since enforcement of boundary conditions and evaluations of nonlinear terms are straightforward. Additionally, some accuracy advantage is seen in the collocation method over the tau method for a number of problems [6] [13]. The series expansion for a function $Q(x)$ may be defined by

$$Q_N(x) = \sum_{n=0}^{\infty} \hat{Q}_n B_n(x),\tag{1}$$

where $B_n(x)$ are the basis functions and N is the total number of nodes employed in the interpolation process (It is also the order of accuracy of the spectral method). The coefficients $\hat{Q}_n$ are often termed the spectrum of $Q_N(x)$. One common technique used to evaluate the spectrum is to consider Equation (1) as an interpolation series representing $Q(x)$. The interpolation "nodes" of such series are the collocation points of the method. For a scheme based on Chebyshev collocation points, the basis functions are:

$$B_n(x) = T_n(x) = 2xP_{n-1}(x) - P_{n-2}(x), n \geq 2,\tag{2}$$

with: $P_0(x) = 1$ and $P_1(x) = x$. The Chebyshev-Gauss-Lobatto standard collocation points are defined by:

$$x_l = \cos\left(\frac{\pi l}{N}\right),\quad l = 0, 1, \cdots, N.\tag{3}$$

The Chebyshev collocation points result from a simple change of variables, which relates the Chebyshev interpolation series to a Fourier cosine series [6, 13]. To evaluate the $\hat{Q}_n$, the inverse relation is required. This is

$$\hat{Q}_n = \hat{c}_n \sum_{l=0}^{N} w_l B_n(x_l) Q_{i,j},\quad n = 0, 1, \cdots,\tag{4}$$

with w_l being a normalized weighting function and $\hat{c}_n$ a constant. These variables assume the following expressions to a Chebyshev-Gauss-Lobatto interpolation:

$$\hat{c}_n = \frac{2}{N\overline{c}_n},\text{ where: } \overline{c}_n = \begin{cases} 2, n = 0 \text{ or } N \\ 1,\ 0 < n < N \end{cases} \text{ and } w_l = \frac{1}{\overline{c}_l}.\tag{5}$$

Legendre collocation is based on using Legendre polynomials as the basis function in Equation (1), e.g.,

$$B_n(x) = \frac{\left[(2n-1)xP_{n-1}(x) - (n-1)P_{n-2}(x)\right]}{n}, n \geq 2,\tag{6}$$

where: $P_0(x) = 1$ and $P_1(x) = x$. Interpolation via Legendre series cannot easily be related to trigonometric interpolation, so there is no simple expression to evaluate the $\hat{Q}_n$ coefficients. Appeal must be made to the theory of numerical quadrature to form an approximation to the integrals which result from analytic Legendre interpolation [14]. Considering Equation (4), the normalized weights and constant of the Legendre-Gauss-Lobatto collocation points are

$$w_l = \frac{1}{N(N+1)B_N^2(x_l)} \text{ and } \hat{c}_n = \begin{cases} 2n+1,\ n = 0, 1, \cdots, (N-1) \\ N,\quad\quad n = N \end{cases}.\tag{7}$$

In this current work, it was assumed that the Legendre-Gauss-Lobatto collocation points are the same as the Chebyshev-Gauss-Lobatto ones. It was also adopted the following collocation points and normalized weight for the Chebyshev-Gauss-Radau interpolation, based on the work of [15]:

$$x_l = \cos\left(\frac{2\pi l}{2N+1}\right), \tag{8}$$

$$w_l = \begin{cases} \dfrac{N}{2N+1}, & l = 0 \\ \dfrac{N}{N+1}, & \text{elsewhere} \end{cases}. \tag{9}$$

For the Legendre-Gauss-Radau interpolation, also based in [15], the collocation points are defined by Equation (8) and the normalized weights are described by:

$$w_l = \begin{cases} \dfrac{1}{(N+1)^2}, & l = 0 \\ \dfrac{1}{2(N+1)^2} \times \dfrac{1-x_l}{B_N^2(x_l)}, & \text{elsewhere} \end{cases}. \tag{10}$$

The same application to the vector of conserved variables Q is applied to the vector of flux C, to be defined in section 5. The proposed method has two collocation point options and two normalized weight functions to be considered by the Chebyshev and Legendre methods: Chebyshev-Gauss-Radau, Chebyshev-Gauss-Lobatto, Legendre-Gauss-Radau and Legendre-Gauss-Lobatto.

3. Reactive Navier-Stokes in 2D

As the Navier-Stokes equations tend to the Euler equations when high Reynolds number are employed, only the former equations are presented. The reactive Navier-Stokes equations in thermochemical non-equilibrium, where the rotational and vibrational contributions are considered, were implemented on conservative and finite volume contexts, in the two-dimensional space. In this case, these equations in integral and conservative forms can be expressed by:

$$\frac{\partial}{\partial t}\int_V Q \mathrm{d}V + \int_S \boldsymbol{F} \cdot \boldsymbol{n}\,\mathrm{d}S = \int_V S_{CVE}\,\mathrm{d}V \text{, with: } \boldsymbol{F} = (E_e - E_v)\boldsymbol{i} + (F_e - F_v)\boldsymbol{j}, \tag{11}$$

where: Q is the vector of conserved variables, V is the volume of a computational cell, $\boldsymbol{F}$ is the complete flux vector, $\boldsymbol{n}$ is the unity vector normal to the flux face, S is the flux area, S_{CVE} is the chemical, vibrational, and electron source term, E_e and F_e are the convective flux vectors or the Euler flux vectors in the x and y directions, respectively, and E_v and F_v are the viscous flux vectors in the x and y directions, respectively. The $\boldsymbol{i}$ and $\boldsymbol{j}$ unity vectors define the Cartesian coordinate system. Twelve (12) conservation equations are solved: one of general mass conservation, two of linear momentum conservation, one of total energy, six of species mass conservation, one of vibrational energy, and one of electron energy. Therefore, one of the species is absent of the iterative process. The CFD literature recommends that the species of biggest mass fraction of the gaseous

mixture should be omitted, aiming to result in a minor numerical accumulation error. To the present study, in which is chosen a chemical model to the air composed of seven (7) species (N, O, N_2, O_2, NO, NO^+, and e^-), this species can be the N_2 or the O_2. To this work, the N_2 was chosen. The vectors Q, E_e, F_e, E_v, F_v, and S_{CVE} can, hence, be defined as follows:

$$Q = \left\{ \begin{array}{c} \rho \\ \rho u \\ \rho v \\ e \\ \rho_1 \\ \rho_2 \\ \rho_4 \\ \rho_5 \\ \rho_6 \\ \rho_7 \\ \rho e_V \\ \rho_e e_e \end{array} \right\}, \quad E_e = \left\{ \begin{array}{c} \rho u \\ \rho u^2 + p \\ \rho uv \\ \rho H u \\ \rho_1 u \\ \rho_2 u \\ \rho_4 u \\ \rho_5 u \\ \rho_6 u \\ \rho_7 u \\ \rho e_V u \\ \rho e_e u \end{array} \right\}, \quad F_e = \left\{ \begin{array}{c} \rho v \\ \rho uv \\ \rho v^2 + p \\ \rho H v \\ \rho_1 v \\ \rho_2 v \\ \rho_4 v \\ \rho_5 v \\ \rho_6 v \\ \rho_7 v \\ \rho e_V v \\ \rho e_e v \end{array} \right\} ; \tag{12}$$

in which: ρ is the mixture density; ρ_e is the electron's density; u and v are Cartesian components of the velocity vector in the x and y directions, respectively; e is the fluid total energy; H is the total enthalpy; ρ_1, ρ_2, ρ_4, ρ_5, ρ_6, and ρ_7 are densities of the N, O, O_2, NO, NO^+, and e^-, respectively; e_V is the sum of the vibrational energy of the molecules N_2, O_2, NO, and NO^+; e_e is the electron's specific energy; the τ's are the components of the viscous stress tensor; f_x and f_y are viscous work and Fourier heat flux functions; $f_{e,x}$ and $f_{e,y}$ are viscous work and Fourier heat flux functions due to the electron; $\rho_s v_{sx}$ and $\rho_s v_{sy}$ represent the species diffusion flux, defined by the Fick law; ϕ_x and ϕ_y are the terms of mixture diffusion; $\phi_{e,x}$ and $\phi_{e,y}$ are the electron's diffusion terms; $\phi_{v,x}$, and $\phi_{v,y}$ are terms of molecular diffusion; $\dot{\omega}_s$ is the chemical source term of each species equation, defined by the law of mass action; $q_{v,x}$ and $q_{v,y}$ are the vibrational Fourier heat flux components in the x and y directions, respectively;

$$E_v = \frac{1}{Re} \left\{ \begin{array}{c} 0 \\ \tau_{xx} \\ \tau_{xy} \\ f_x - \phi_x \\ -\rho_1 v_{1x} \\ -\rho_2 v_{2x} \\ -\rho_4 v_{4x} \\ -\rho_5 v_{5x} \\ -\rho_6 v_{6x} \\ -\rho_7 v_{7x} \\ q_{v,x} - \phi_{v,x} \\ f_{e,x} - \phi_{e,x} \end{array} \right\}, \quad F_v = \frac{1}{Re} \left\{ \begin{array}{c} 0 \\ \tau_{xy} \\ \tau_{yy} \\ f_y - \phi_y \\ -\rho_1 v_{1y} \\ -\rho_2 v_{2y} \\ -\rho_4 v_{4y} \\ -\rho_5 v_{5y} \\ -\rho_6 v_{6y} \\ -\rho_7 v_{7y} \\ q_{v,y} - \phi_{v,y} \\ f_{e,y} - \phi_{e,y} \end{array} \right\} ; \tag{13}$$

$Q_{T\text{-}V}$ is the translation-vibration energy transfer rate for the diatomic molecules; $S_{e,pg}$, $S_{e,trans}$, $S_{e,inel}$ and $S_{e,chem}$ are the electron's relaxation source terms; and Re is the laminar Reynolds number. In Equation (12), the pressure term of the electron's convective flux balance was suppressed aiming to simplify the computational implementation as well reduce the computational cost.

$$S_{CVE} = \begin{Bmatrix} 0 \\ 0 \\ 0 \\ 0 \\ \dot{\omega}_1 \\ \dot{\omega}_2 \\ \dot{\omega}_4 \\ \dot{\omega}_5 \\ \dot{\omega}_6 \\ \dot{\omega}_7 \\ Q_{T\text{-}V} + \sum_{s=mol} \dot{\omega}_s e_{v,s} \\ S_{e,pg} + S_{e,trans} + S_{e,inel} + S_{e,chem} \end{Bmatrix}. \tag{14}$$

The viscous stresses, in N/m^2, are determined, according to a Newtonian fluid model, by:

$$\tau_{xx} = 2\mu_m \frac{\partial u}{\partial x} - \frac{2}{3}\mu_m \left(\frac{\partial u}{\partial x} + \frac{\partial v}{\partial y} \right);$$

$$\tau_{xy} = \mu_m \left(\frac{\partial u}{\partial y} + \frac{\partial v}{\partial x} \right); \tag{15}$$

$$\tau_{yy} = 2\mu_m \frac{\partial v}{\partial y} - \frac{2}{3}\mu_m \left(\frac{\partial u}{\partial x} + \frac{\partial v}{\partial y} \right).$$

where μ_m is the molecular viscosity. Expressions to f_x and f_y are given below:

$$f_x = \tau_{xx} u + \tau_{xy} v + q_x + q_{e,x} + q_{v,x}; \tag{16}$$

$$f_y = \tau_{xy} u + \tau_{yy} v + q_y + q_{e,y} + q_{v,y}, \tag{17}$$

where q_x and q_y are the Fourier heat flux components and are given by:

$$q_x = k \frac{\partial T}{\partial x} \quad \text{and} \quad q_y = k \frac{\partial T}{\partial y}, \tag{18}$$

where: k is the thermal conductivity due to translation and rotation. The $q_{v,x}$ and $q_{v,y}$ are the vibrational heat flux components and are given by:

$$q_{v,x} = k_v \frac{\partial T_v}{\partial x} \quad \text{and} \quad q_{v,y} = k_v \frac{\partial T_v}{\partial y}, \tag{19}$$

with k_v being the mixture-vibrational-thermal conductivity, and T_V is the vibrational temperature. The electron's Fourier heat flux is determined by:

$$q_{e,x} = k_e \frac{\partial T_e}{\partial x} \quad \text{and} \quad q_{e,y} = k_e \frac{\partial T_e}{\partial y}, \tag{20}$$

where T_e is the electron's temperature and k_e is the electron's thermal conductiv-

ity. The terms of species diffusion, defined by the Fick law, to a condition of thermal non-equilibrium, are determined by [16]:

$$\rho_s v_{sx} = -\rho D_s \frac{\partial Y_{MF,s}}{\partial x} \quad \text{and} \quad \rho_s v_{sy} = -\rho D_s \frac{\partial Y_{MF,s}}{\partial y}, \tag{21}$$

with "s" referent to a given species, $Y_{MF,s}$ being the molar fraction of the species, defined as:

$$Y_{MF,s} = \frac{\dfrac{\rho_s}{M_s}}{\sum_{k=1}^{ns} \dfrac{\rho_k}{M_k}} \tag{22}$$

and D_s is the species-effective-diffusion coefficient. "ns" is the number of species. The diffusion terms ϕ_x and ϕ_y, which appear in the energy equation, are defined by [17]:

$$\phi_x = \sum_{s=1}^{ns} \rho_s v_{sx} h_s \quad \text{and} \quad \phi_y = \sum_{s=1}^{ns} \rho_s v_{sy} h_s, \tag{23}$$

being h_s the specific enthalpy (sensible) of the chemical species "s". The molecular diffusion terms calculated at the vibrational temperature, $\phi_{v,x}$ and $\phi_{v,y}$, which appear in the vibrational-internal-energy equation are defined by ([16]):

$$\phi_{v,x} = \sum_{s=mol} \rho_s v_{sx} h_{v,s} \quad \text{and} \quad \phi_{v,y} = \sum_{s=mol} \rho_s v_{sy} h_{v,s}, \tag{24}$$

with $h_{v,s}$ being the specific enthalpy (sensible) of the chemical species "s" calculated at the vibrational temperature T_V. The sum of Equation (24), as also those present in Equation (14), considers only the molecules of the system, namely: N_2, O_2, NO, and NO^+. The laminar Reynolds number is estimated by:

$$Re = \frac{\rho_{char} V_{initial} L_{REF}}{\mu_{m,char}}, \tag{25}$$

with "$char$" related to characteristic or freestream variables, $V_{initial}$ is the flow initial velocity, and L_{REF} a characteristic configuration length. For details of the chemical model, the calculation of thermodynamic and transport properties see [18] [19].

For the electron energy equation, the following expressions are defined to $f_{e,x}$ and $f_{e,y}$:

$$f_{e,x} = \tau_{xx,e} u + \tau_{xy,e} v + q_{e,x} \quad \text{and} \quad f_{e,y} = \tau_{xy,e} u + \tau_{yy,e} v + q_{e,y}, \tag{26}$$

where the electron viscous stresses are calculated with the Equation (15), being the electron's molecular viscosity used in place of the mixture molecular viscosity. The electron's diffusion flux is given by:

$$\phi_{e,x} = \rho_e v_{ex} e_e \quad \text{and} \quad \phi_{e,y} = \rho_e v_{ey} e_e. \tag{27}$$

The caloric equation of state for the mass-averaged gas is derived subtracting the vibrational, kinetic, electron, and chemical energies from the total energy to yield the energy in the translational and rotational modes [20]. Assuming that the rotational energy modes are in equilibrium with the translational modes, it is

possible to determine the translational-rotational temperature T,

$$\sum_{r \neq e} \rho_r c_{v,r} T = e - \frac{1}{2} \sum_{r \neq e} \rho_r \left(u^2 + v^2\right) - \sum_{s=mol} \rho_s e_{v,s} - \rho_e e_e - \sum_r \rho_r h_r^0 , \quad (28)$$

where h^0 is the formation enthalpy. The pressure is the sum of the partial pressures,

$$p = \sum_{r \neq e} \rho_r R_r T + p_e , \quad (29)$$

being p_e the electron's pressure. The equations of state for the electrons are

$$\rho_e c_{v,e} T_e = \rho_e e_e - \frac{1}{2} \rho_e \left(u^2 + v^2\right) \quad \text{and} \quad p_e = \rho_e R_e T_e . \quad (30)$$

It was assumed that the energy contained in the excited electronic states of the molecules is negligible relative to the energy contained in the other modes.

4. Energy Exchange Mechanisms

The energy exchange mechanisms that appear on the S_{CVE} term must be modeled. The models are described below, based on [20] work.

4.1. Translation-Vibration Energy Exchanges

The rates of energy exchange between the translational and vibrational modes Q_{T-V} are assumed to be of the Landau-Teller form,

$$Q_{T-Vs} = \rho_s \frac{e_{vs}^*(T) - e_{vs}}{\langle \tau_s \rangle} , \quad (31)$$

with T the translational-rotational temperature. The Landau-Teller relaxation time is given by an expression from [21],

$$\langle \tau_s \rangle = \frac{\sum_r X_r}{\sum_r \dfrac{X_r}{\tau_{sr}}} , \text{ for } r \neq e , \quad (32)$$

where X_r is the mole fraction and τ_{sr} is given by:

$$\tau_{sr} = \frac{B}{p_s} e^{\left[A\left(T^{-1/3} - 0.015 \mu_{sr}^{0.25}\right) - 18.42\right]} , \quad (33)$$

with $B = 1.013 \times 10^5$ Pa.s, p_s is the species pressure in Pa, A is defined in [18] [19], $\mu_{sr} = \dfrac{M_s M_r}{M_s + M_r}$ (the reduced mass), and M_s the molecular weight.

4.2. Electron Pressure Gradient, $S_{e,pg}$

This term is an approximation to the work done on electrons by the electric field induced by the electron pressure gradient [22]. Its expression is given by:

$$S_{e,pg} = -p_e \left(\frac{\partial u}{\partial x} + \frac{\partial v}{\partial y}\right) . \quad (34)$$

4.3. Translational-Electron Relaxation, $S_{e,trans}$

Energy exchange between translational and electron energies [20] [22]. This term is defined by:

$$S_{e,trans} = 3\rho_e R_{univ} \left(T - T_e\right) \sqrt{\frac{8 R_e T_e}{\pi}} \sum_{r \neq e} \frac{\rho_r N_{Av}}{M_r^2} \sigma_{er} \tag{35}$$

where σ_{er}, $r \neq$ ions, are the collision cross sections for the electron-neutral interations, given in this work by:

$$\sigma_{er} = a_r + b_r T_e + c_r T_e^2 , \tag{36}$$

with model constants defined in Table 1. For the case of electron-ion interactions, the effective Coulomb cross section is determined by:

$$\sigma_{e,ions} = \frac{8\pi}{27} \frac{e^4}{\left(kT_e\right)^2} \ln\left[1 + \frac{9\left(kT_e\right)^3}{4\pi N_e e^6}\right], \tag{37}$$

with "e" being the electron charge (1.6022×10^{-19} C), N_e is the electron's density number, and k the Boltzmann constant.

4.4. Rotational-Electron Relaxation, S_{inel}

This term is related to the inelastic energy exchange between electrons and molecules [22]. The energy relaxation between the rotational and electron energies should be considered in the electron energy equation because of the electron interactions with molecular multipoles. In order to simplify the relaxation term, an energy transfer rate factor, $g_{rot,r}$, can be employed in the expression of the rotational electron energy transfer rate. The rate factor is the ratio of the rotational-electron energy relaxation time to the translational-electron energy relaxation time for the molecular species. Therefore, the relaxation between rotational and electron energies can be expressed in the following form:

$$S_{e,rot} = 3\rho_e R_{univ} \left(T - T_e\right) \sqrt{\frac{8 R_e T_e}{\pi}} \sum_{r \neq e} g_{rot,r} \frac{\rho_r N_{Av}}{M_r^2} \sigma_{er} . \tag{38}$$

For neutral species, the energy transfer rate factor is listed in Table 2. For molecular ions, we assume they have the same rate factor as their neutral molecules.

4.5. Electron Energy Due to Chemical Reactions

The chemistry related term gives added or removed electron energy by chemical reactions and can be expressed as:

$$S_{e,chem} = \dot{\omega}_e e_e . \tag{39}$$

Table 1. The coefficients of the electron-neutral collisional cross section.

Species	a_r	b_r	c_r
N	5.0×10^{-20}	0	0
O	1.2×10^{-20}	1.7×10^{-24}	-2.0×10^{-29}
N_2	7.5×10^{-20}	5.5×10^{-24}	-1.0×10^{-28}
O_2	2.0×10^{-20}	6.0×10^{-24}	0
NO	1.0×10^{-19}	0	0

Table 2. The transfer energy rate factors of rotational-electron energy relaxation.

Species	g_{rot}
N_2	10
O_2	10
NO	100
NO^+	100

5. Numerical Algorithms

Considering the two-dimensional and structured case, the flux vector splitting algorithms follow that described in [7] [8] [9] [18] [19].

5.1. Van Leer and Liou and Steffen Jr. Schemes

The system is solved in three parts separately, according to [23]. The first part takes into account the dynamic part, which considers the Navier-Stokes equations plus the electron energy equation, the second one takes into account the chemical part involving the chemical contributions, and finally, the third part considers only the vibrational contribution. Hence, the discrete-dynamic-convective flux, which solves the dynamic part, is given by:

$$
R_{i+1/2,j}^{Dyn} = \left. |S| \right|_{i+1/2,j} \left\{ \frac{1}{2} M_{i+1/2,j} \left[\begin{pmatrix} \rho a \\ \rho a u \\ \rho a v \\ \rho a H \\ \rho a e_e \end{pmatrix}_L + \begin{pmatrix} \rho a \\ \rho a u \\ \rho a v \\ \rho a H \\ \rho a e_e \end{pmatrix}_R \right] \right.
$$
$$
\left. - \frac{1}{2} \phi_{i+1/2,j} \left[\begin{pmatrix} \rho a \\ \rho a u \\ \rho a v \\ \rho a H \\ \rho a e_e \end{pmatrix}_R - \begin{pmatrix} \rho a \\ \rho a u \\ \rho a v \\ \rho a H \\ \rho a e_e \end{pmatrix}_L \right] \right\} + \begin{pmatrix} 0 \\ S_x p \\ S_y p \\ 0 \\ 0 \end{pmatrix}_{i+1/2,j} \tag{40}
$$

the discrete-chemical-convective flux is defined by:

$$
R_{i+1/2,j}^{Chem} = \left. |S| \right|_{i+1/2,j} \left\{ \frac{1}{2} M_{i+1/2,j} \left[\begin{pmatrix} \rho_1 a \\ \rho_2 a \\ \rho_4 a \\ \rho_5 a \\ \rho_6 a \\ \rho_7 a \end{pmatrix}_L + \begin{pmatrix} \rho_1 a \\ \rho_2 a \\ \rho_4 a \\ \rho_5 a \\ \rho_6 a \\ \rho_7 a \end{pmatrix}_R \right] \right.
$$
$$
\left. - \frac{1}{2} \phi_{i+1/2,j} \left[\begin{pmatrix} \rho_1 a \\ \rho_2 a \\ \rho_4 a \\ \rho_5 a \\ \rho_6 a \\ \rho_7 a \end{pmatrix}_R - \begin{pmatrix} \rho_1 a \\ \rho_2 a \\ \rho_4 a \\ \rho_5 a \\ \rho_6 a \\ \rho_7 a \end{pmatrix}_L \right] \right\} \tag{41}
$$

and finally the discrete-vibrational-convective flux is given by:

$$
\begin{aligned}
R_{i+1/2,j}^{Vib} = |S|_{i+1/2,j} &\left\{ \frac{1}{2} M_{i+1/2,j} \left[(\rho e_v a)_L + (\rho e_v a)_R \right] \right. \\
&\left. - \frac{1}{2} \phi_{i+1/2,j} \left[(\rho e_v a)_R - (\rho e_v a)_L \right] \right\}
\end{aligned}
\tag{42}
$$

where: $S_{i+1/2,j} = \begin{bmatrix} S_x & S_y \end{bmatrix}_{i+1/2,j}^{\mathrm{T}}$ defines the normal area vector for the surface $(i+1/2, j)$, and the speed of sound is defined by the following expression:

$$
a = \sqrt{(\beta+1)\frac{p}{\rho}},
\tag{43}
$$

with β a parameter to be defined, calculated at each interaction. The normal area components S_x and S_y to each flux interface are given in **Table 3**. **Figure 1** exhibits the computational cell adopted for the simulations, as well its respective nodes and flux interfaces.

The same definitions presented in [7] [8] [18] [19] are valid to these algorithms. The definition of the dissipation term ϕ determines the particular formulation of the convective fluxes. The choice below corresponds to the [7] scheme, according to [24]:

$$
\phi_{i+1/2,j} = \phi_{i+1/2,j}^{VL} = \begin{cases}
\left| M_{i+1/2,j} \right|, & \text{if } \left| M_{i+1/2,j} \right| \geq 1; \\
\left| M_{i+1/2,j} \right| + 0.5(M_R - 1)^2, & \text{if } 0 \leq M_{i+1/2,j} < 1; \\
\left| M_{i+1/2,j} \right| + 0.5(M_L + 1)^2, & \text{if } -1 < M_{i+1/2,j} \leq 0.
\end{cases}
\tag{44}
$$

and the [8] scheme is obtained by, according to [24]:

$$
\phi_{i+1/2,j} = \phi_{i+1/2,j}^{LS} = \left| M_{i+1/2,j} \right|,
\tag{45}
$$

with M being the Mach number and R and L right and left states. Both schemes

Table 3. Values of S_x and S_y.

Surface	S_x	S_y
$i, j-1/2$	$y_{i+1,j} - y_{i,j}$	$x_{i,j} - x_{i+1,j}$
$i+1/2, j$	$y_{i+1,j+1} - y_{i+1,j}$	$x_{i+1,j} - x_{i+1,j+1}$
$i, j+1/2$	$y_{i,j+1} - y_{i+1,j+1}$	$x_{i+1,j+1} - x_{i,j+1}$
$i-1/2, j$	$y_{i,j} - y_{i,j+1}$	$x_{i,j+1} - x_{i,j}$
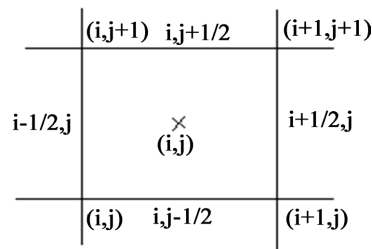
Figure 1. Computational cell.

are first-order accurate in space and in time. The high-order spatial accuracy is obtained, in the current study, by the spectral method.

5.2. Steger and Warming Scheme

The [9] scheme was also implemented in the present work. The U contravariant velocity defined by the [9] scheme is

$$U = un_x + vn_y .$$ (46)

The eigenvalues of the Euler equations are defined as

$$\lambda_1 = U , \quad \lambda_2 = U + a \quad \text{and} \quad \lambda_3 = U - a .$$ (47)

The separated eigenvalues, based on the work of [9], which defines positive and negative contributions, can be expressed as

$$\lambda_1^+ = \frac{1}{2}\left(\lambda_1 + \sqrt{\lambda_1^2 + \varepsilon^2}\right), \quad \lambda_2^+ = \frac{1}{2}\left(\lambda_2 + \sqrt{\lambda_2^2 + \varepsilon^2}\right);$$ (48)

$$\lambda_3^+ = \frac{1}{2}\left(\lambda_3 + \sqrt{\lambda_3^2 + \varepsilon^2}\right), \quad \lambda_1^- = \frac{1}{2}\left(\lambda_1 - \sqrt{\lambda_1^2 + \varepsilon^2}\right);$$ (49)

$$\lambda_2^- = \frac{1}{2}\left(\lambda_2 - \sqrt{\lambda_2^2 + \varepsilon^2}\right), \quad \lambda_3^- = \frac{1}{2}\left(\lambda_3 - \sqrt{\lambda_3^2 + \varepsilon^2}\right),$$ (50)

where ε is a small parameter, adopted as 0.04.

The coefficients of the [9] scheme, which defines the separated numerical flux vectors, are determined in **Table 4**. Six coefficients were defined. These coefficients were prescribed in terms of thermodynamic and sound speed variables.

The numerical flux vector was decomposed in three components, based on the dynamic, chemical, and vibrational parcels of the flow. The flux vector to each parcel is separated in positive and negative contributions, based on the homogeneity property of the Euler flux vectors. For the dynamic parcel, where it was included the electron energy equation, one has:

Table 4. Coefficients of the Steger and Warming scheme.

Coefficient	Expression
C_1	$\dfrac{p}{a^2}\beta$
C_2	$\dfrac{\rho}{2a^2}\left(a^2 - \dfrac{p}{\rho}\beta\right)$
C_3	$e - \dfrac{H}{\rho a^2}\left(\rho a^2 - p\beta\right)$
C_4	$\dfrac{H + aU}{2a^2}\left(\rho a^2 - p\beta\right)$
C_5	$\dfrac{H - aU}{2a^2}\left(\rho a^2 - p\beta\right)$
C_6	$\dfrac{1}{2a^2}\left(\rho a^2 - p\beta\right)$

$$F_{Dyn}^{\pm} = \left\{ \begin{array}{c} C_1\lambda_1^{\pm} + C_2\lambda_2^{\pm} + C_2\lambda_3^{\pm} \\ C_1\lambda_1^{\pm}u + C_2\lambda_2^{\pm}\left(u + an_x\right) + C_2\lambda_3^{\pm}\left(u - an_x\right) \\ C_1\lambda_1^{\pm}v + C_2\lambda_2^{\pm}\left(v + an_y\right) + C_2\lambda_3^{\pm}\left(v - an_y\right) \\ C_3\lambda_1^{\pm} + C_4\lambda_2^{\pm} + C_5\lambda_3^{\pm} \\ \left(C_1\lambda_1^{\pm} + C_6\lambda_2^{\pm} + C_6\lambda_3^{\pm}\right)e_e \end{array} \right\} ; \qquad (51)$$

For the chemical parcel, one has for the six equations, the following numerical flux vector, where c_s is the mass fraction and is numbered from 1 to 7, except the number 3, which is associated to the N_2 species.

$$F_{Chem}^{\pm} = \left\{ \begin{array}{c} \left(C_1\lambda_1^{\pm} + C_2\lambda_2^{\pm} + C_2\lambda_3^{\pm}\right)c_{s,1} \\ \left(C_1\lambda_1^{\pm} + C_2\lambda_2^{\pm} + C_2\lambda_3^{\pm}\right)c_{s,2} \\ \left(C_1\lambda_1^{\pm} + C_2\lambda_2^{\pm} + C_2\lambda_3^{\pm}\right)c_{s,4} \\ \left(C_1\lambda_1^{\pm} + C_2\lambda_2^{\pm} + C_2\lambda_3^{\pm}\right)c_{s,5} \\ \left(C_1\lambda_1^{\pm} + C_2\lambda_2^{\pm} + C_2\lambda_3^{\pm}\right)c_{s,6} \\ \left(C_1\lambda_1^{\pm} + C_2\lambda_2^{\pm} + C_2\lambda_3^{\pm}\right)c_{s,7} \end{array} \right\} ; \qquad (52)$$

Finally, the vibrational component is defined by the following equation:

$$F_{Vib}^{\pm} = \left\{ \left(C_1\lambda_1^{\pm} + C_6\lambda_2^{\pm} + C_6\lambda_3^{\pm}\right)e_v \right\} , \qquad (53)$$

where e_v is the vibrational energy. For the positive components of the flux vectors, the cell properties are employed, whereas for the negative components the neighboring cell properties are used.

The viscous formulation follows that of [25], which adopts the Green theorem to calculate primitive variable gradients. The viscous gradients at the flux interface are obtained by arithmetical average between cell (i,j) and its neighbors. As was done with the convective terms, there is a need to separate the viscous flux in three parts: dynamic viscous flux, chemical viscous flux, and vibrational viscous flux. The dynamic part corresponds to the first four equations of the Navier-Stokes ones plus the electron equation, the chemical part corresponds to the six equations immediately below the electron energy equation, and the vibrational part corresponds to the one that follows the last chemical equation. The resultant ordinary differential equation system can be written as:

$$V_{i,j}\frac{dQ_{i,j}}{dt} = -\left(R_{i,j-1/2} + R_{i+1/2,j} + R_{i,j+1/2} + R_{i-1/2,j}\right) = -C_{i,j} , \qquad (54)$$

where $R_{i+1/2,j} = R_{i+1/2,j}^{Dyn} + R_{i+1/2,j}^{Chem} + R_{i+1/2,j}^{Vib}$, and the cell volume is given by:

$$\begin{aligned} V_{i,j} = &0.5\left|\left(x_{i,j} - x_{i+1,j}\right)y_{i+1,j+1} + \left(x_{i+1,j} - x_{i+1,j+1}\right)y_{i,j} + \left(x_{i+1,j+1} - x_{i,j}\right)y_{i+1,j}\right| \\ &+ 0.5\left|\left(x_{i,j} - x_{i+1,j+1}\right)y_{i,j+1} + \left(x_{i+1,j+1} - x_{i,j+1}\right)y_{i,j} + \left(x_{i,j+1} - x_{i,j}\right)y_{i+1,j+1}\right| \end{aligned} \qquad (55)$$

For the [7] and [8] schemes, Equation (54) can be used directly. For the [9] scheme, however, the R components are calculated by the following equation, considering the dynamic contribution:

$$R_{i,j-1/2}^{Dyn} = F_{Dyn}^{+}\left(Q^{-}\right) + F_{Dyn}^{-}\left(Q^{+}\right), \tag{56}$$

where Q^{-} and Q^{+} are computed considering Q^{-} the cell properties and Q^{+} the neighboring cell properties.

In the present study, the Euler backward method was employed to march the scheme in time. This method is first-order accurate in time, to the three types of complete flux. To the convective dynamic component, this method can be represented in general form by:

$$Q_{i,j}^{(n+1)} = Q_{i,j}^{(n)} - \Delta t_{i,j} \times \left\{ \frac{C\left[Q_{i,j}^{(n)}\right]}{V_{i,j}} - S_E\left[Q_{i,j}^{(n)}\right] \right\}, \tag{57}$$

with S_E being the modified electron source term, composed by the last line in Equation (14). To the convective chemical part, it can be represented in general form by:

$$Q_{i,j}^{(n+1)} = Q_{i,j}^{(n)} - \Delta t_{i,j} \times \left\{ \frac{C\left[Q_{i,j}^{(n)}\right]}{V_{i,j}} - S_C\left[Q_{i,j}^{(n)}\right] \right\}, \tag{58}$$

where the chemical source term S_C is defined by Equation (14) and is calculated with the temperature Trrc (reaction rate control temperature, see [18] [19]). Finally, to the convective vibrational component, where S_V is defined by Equations (14) and (31), one has:

$$Q_{i,j}^{(n+1)} = Q_{i,j}^{(n)} - \Delta t_{i,j} \times \left\{ \frac{C\left[Q_{i,j}^{(n)}\right]}{V_{i,j}} - S_V\left[Q_{i,j}^{(n)}\right] \right\}. \tag{59}$$

6. Spatially Variable Time Step

The spatially variable time step has proved efficient gains in terms of convergence acceleration, as verified by [10] [11]. Initially, the parameter σ is determined, where:

$$\sigma_s = \frac{c_s}{M_s} \quad \text{and} \quad \sigma = \sum_{s=1}^{ns} \sigma_s, \tag{60}$$

with c_s being the mass fraction and M_s the molecular weight. The total specific heat at constant volume due to translation is defined as:

$$c_{v,t} = \sum_{s=1}^{ns} \sigma_s c_{v,t,s}, \tag{61}$$

where, for each gas constituent of the seven (7) species chemical model, the specific heat at constant volume, based on the kinetic theory of gases ([26]), is defined by

$$c_{v,t,N} = \frac{3}{2}R_N, \quad c_{v,t,O} = \frac{3}{2}R_O, \quad c_{v,t,N_2} = \frac{5}{2}R_{N_2}, \quad c_{v,t,O_2} = \frac{5}{2}R_{O_2}; \tag{62}$$

$$c_{v,t,NO} = \frac{5}{2}R_{NO}, \quad c_{v,t,NO^+} = \frac{5}{2}R_{NO^+} \quad \text{and} \quad c_{v,t,e^-} = \frac{3}{2}R_{e^-}. \tag{63}$$

being R_s the specific gas constant. The total pressure of the gaseous mixture is determined by Dalton law, which indicates that the total pressure of the gas is the sum of the partial pressure of each constituent gas, resulting in:

$$p_s = c_s \rho R_s T \quad \text{and} \quad p = \sum_{s=1}^{ns-1} p_s + p_e , \tag{64}$$

where $s = 7$ is related to the electron. The speed of sound to a reactive mixture considering thermochemical non-equilibrium is given by Equation (43), where

$\beta = \dfrac{R_{univ}\sigma}{c_{v,t}}$, with $R_{univ} = 1.987$ cal/(g-mol.K). Finally, the spatially variable time step is defined from the CFL definition:

$$\Delta t_{i,j} = \frac{\text{CFL}\Delta s_{i,j}}{\sqrt{u_{i,j}^2 + v_{i,j}^2} + a_{i,j}} , \tag{65}$$

where $\Delta s_{i,j}$ is the characteristic length of each cell (defined between the minimum cell side and the minimum centroid distance between each cell and its neighbors).

7. Results

The initial conditions to the circumference, to the reentry capsule, to the blunt body, and to the double ellipse problems, for a seven species chemical model, are presented in **Table 5**. The Reynolds number is obtained from data of [27].

Tests were performed in a Core i7 processor of 2.8 GHz and 6.0 Gbytes of RAM microcomputer, in a Windows 10.0 environment. Three (3) orders of reduction of the maximum residual in the field were considered to obtain a converged solution. The residual was defined as the value of the discretized conservation equation.

Table 5. Initial conditions to the four problems studied in this work.

Property	Circumfernce	Reentry Capsule	Blunt Body	Double Ellipse
M_∞	14.8	10.6	8.78	15.0
ρ_∞	0.007291 kg/m³	0.02863 kg/m³	0.00326 kg/m³	0.00922 kg/m³
p_∞	664 Pa	3885 Pa	687 Pa	794 Pa
U_∞	5280 m/s	4628 m/s	4776 m/s	5208 m/s
T_∞	293 K	473 K	694 K	300 K
$T_{V,\infty}$	293 K	473 K	694 K	300 K
Altitude	50,000 m	40,000 m	40,000 m	50,000 m
c_N	10^{-9}	10^{-9}	10^{-9}	10^{-9}
c_O	0.07955	0.07955	0.07955	0.07955
c_{O_2}	0.13400	0.13400	0.13400	0.13400
c_{NO}	0.05090	0.05090	0.05090	0.05090
c_{NO+}	0.0	0.0	0.0	0.0
c_{e-}	10^{-9}	10^{-9}	10^{-9}	10^{-9}
L_{REF}	2.0 m	3.0 m	2.0 m	5.0 m

The attack angle was adopted equal to zero. For a matter of simplicity, the following abbreviations were used: [7] scheme = VL, [8] scheme = LS, [9] scheme = SW, Chebyshev-Gauss-Radau = CGR. Only some results obtained with these configurations are presented in this section. Converged results involve second to fifth orders accuracy and eighth and sixteenth orders of accuracy. It is presented the pressure contours, the translational/rotational temperature contours, electron temperature contours and temperature distributions at the body wall (translational/rotational, vibrational and electron temperatures).

7.1. Circumference

The first studied problem is the circumference configuration. Only the SW scheme has presented converged results for the inviscid case. Their solutions are presented in relation to the four types of results described above.

Figures 2-5 present the 2nd order SW solutions in the CGR variant of the
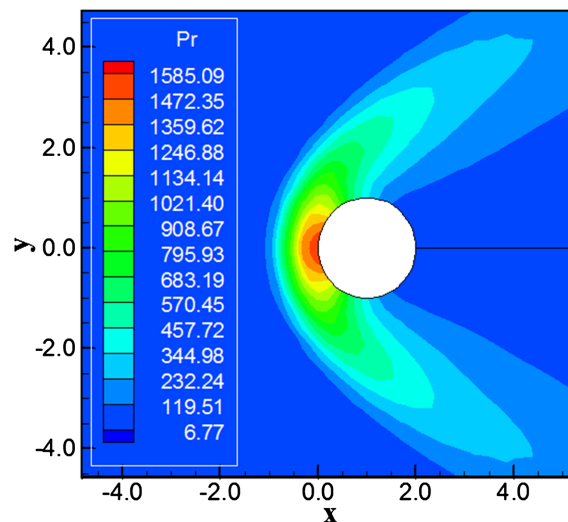
Figure 2. Pressure contours (SW-CGR-2nd).
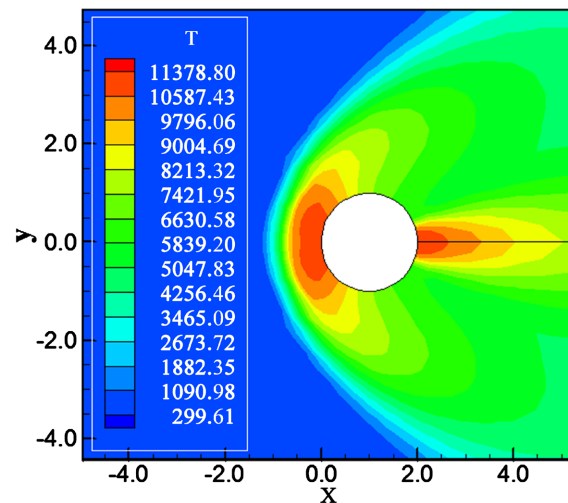
Figure 3. Temperature contours (SW-CGR-2nd).
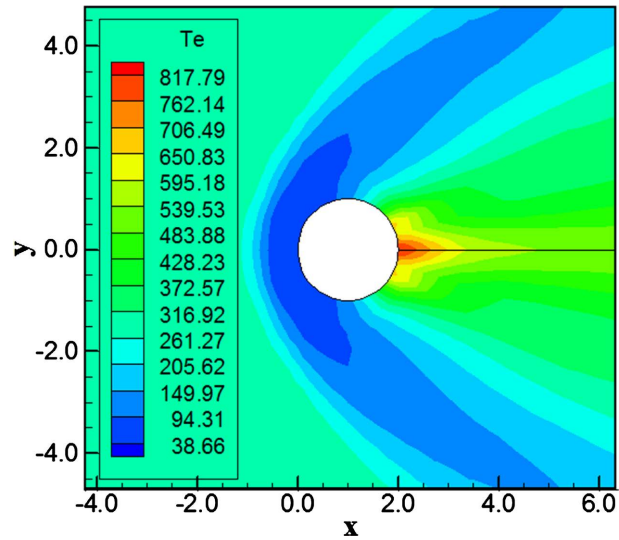
Figure 4. Electron temperature contours (SW-CGR-2nd).
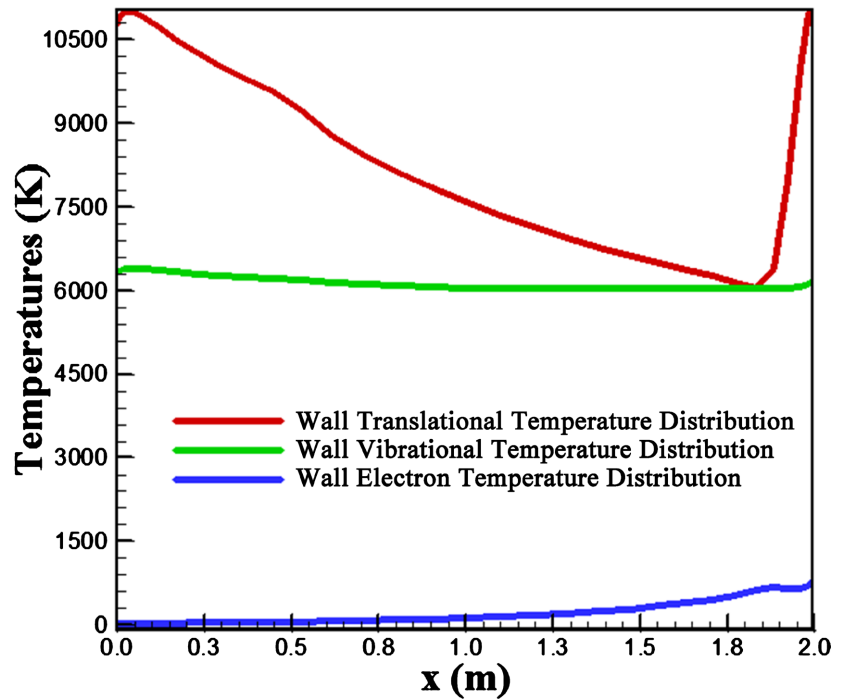
Figure 5. Wall temperature distributions (SW-CGR-2nd).

proposed spectral method. The stagnation pressure was estimated in 1585.09 units. The maximum translational/rotational temperature was 11,378.80 K. The maximum electron temperature was 817.79 K. Good symmetrical properties are observed in all contours.

The temperature distributions show that the vibrational temperature remains practically constant along the body wall. The electron temperature has an increasing behavior close to the circumference's trailing edge. The translational/rotational temperature has a decreasing behavior along the body, increasing close to the trailing edge.

7.2. Reentry Capsule

For this problem, the inviscid solutions are described. The VL and SW schemes have presented converged results and only the CGR variant solutions of the spectral method are exhibited for the VL scheme.

Figures 6-9 present the 3rd order VL solutions for the four types of results described above. The maximum pressure, stagnation pressure, was calculated in 1494.54 unities, at the body's nose, and the maximum translational/rotational temperature, the stagnation temperature, was observed in 9364.49 K. The temperature distributions present the quasi-constant vibrational behavior and the increase of the electron temperature along the body.
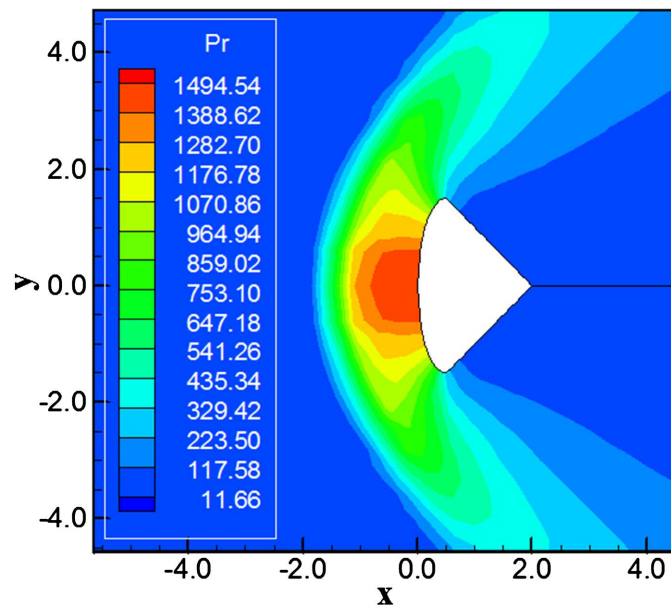
Figure 6. Pressure contours (VL-CGR-3rd).
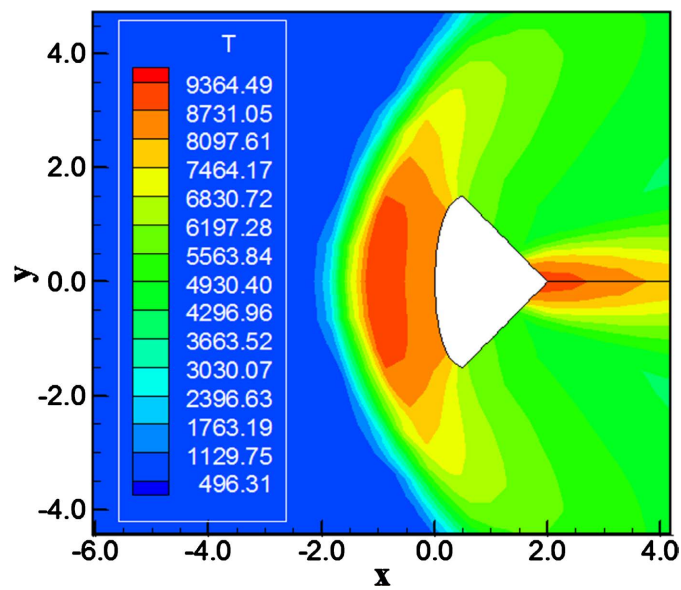
Figure 7. Temperature contours (VL-CGR-3rd).
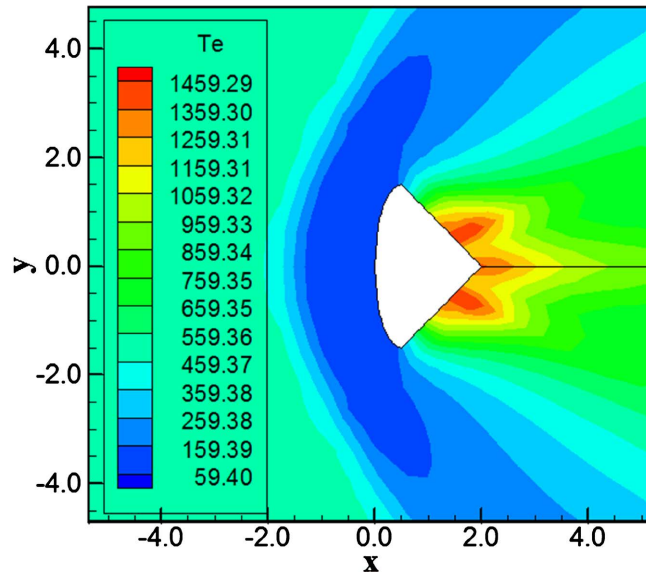
Figure 8. Electron temperature contours (VL-CGR-3rd).
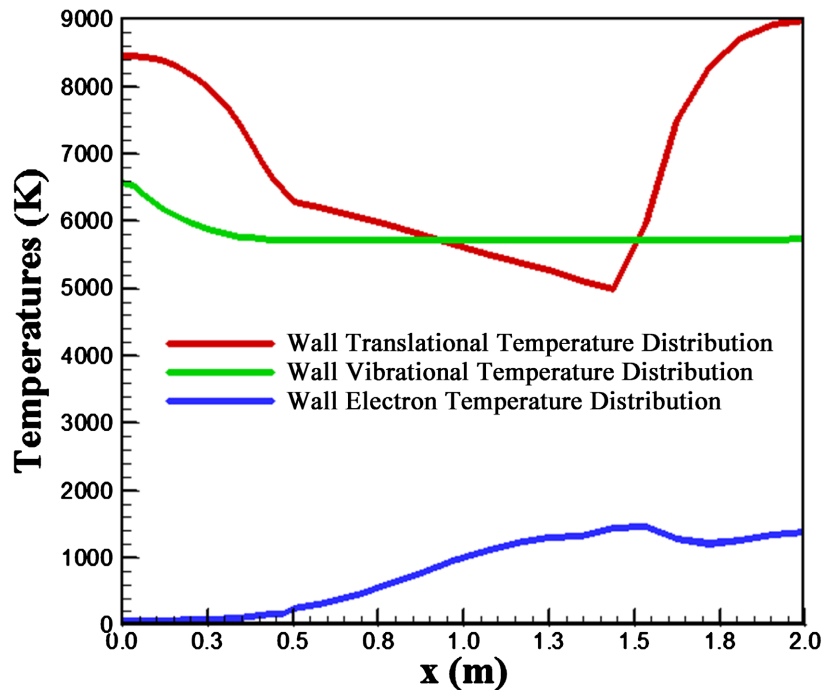
Figure 9. Wall temperature distributions (VL-CGR-3rd).

7.3. Blunt Body Problem

Solutions of second, third, fourth, fifth, eighth and sixteenth orders of accuracy are obtained with the Spectral method for the inviscid and viscous cases.

Inviscid Case. Figures 10-13 exhibit the pressure and temperature contours as well the temperature distribution profiles along the body's wall obtained with the SW scheme as using the Spectral method of fourth order of accuracy, with CGR weighting function. The maximum pressure is obtained at the body's nose with the value of 141.94 unities, whereas the maximum temperature is obtained
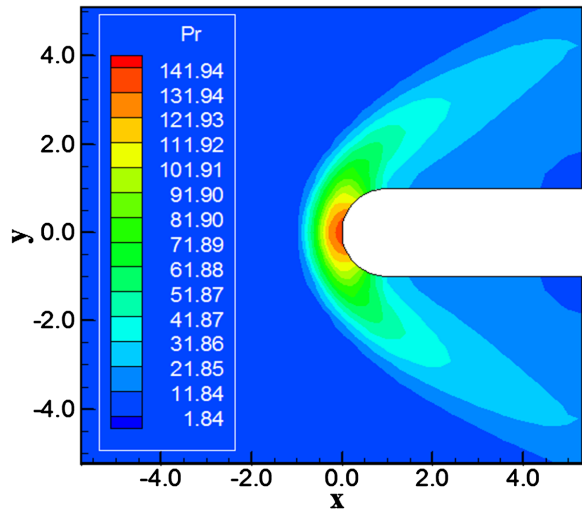
Figure 10. Pressure contours (SW-CGR-4th).
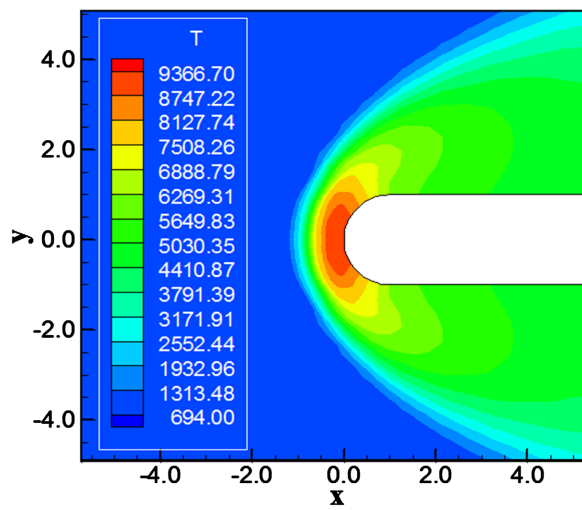
Figure 11. Temperature contours (SW-CGR-4th).
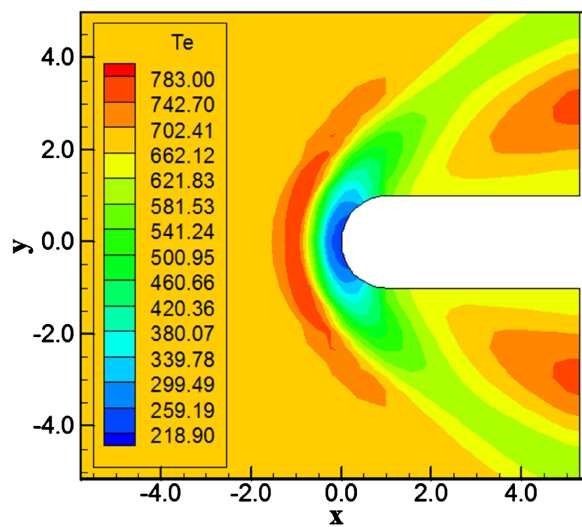
Figure 12. Electron temperature contours (SW-CGR-4th).

with the value of 9366.70 K. The maximum electron temperature is obtained with the value of 783.00 K. The wall temperature profiles are shown at **Figure 13**. In this figure the vibrational temperature is not constant and has a decreasing behavior. The electron profile has a typical constant profile along the wall. The translational/rotational temperature profile reaches a minimum at the body's end, close to 5000 K. The solutions are symmetrical in relation to the body's symmetry line.

Viscous Case. **Figures 14-17** present the pressure and the temperature contours
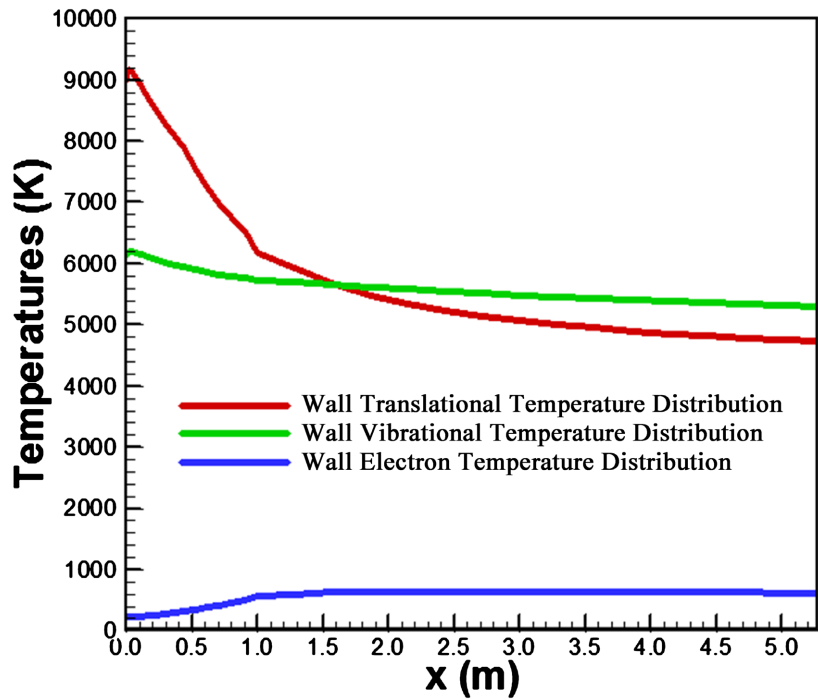
Figure 13. Wall temperature distributions (SW-CGR-4th).
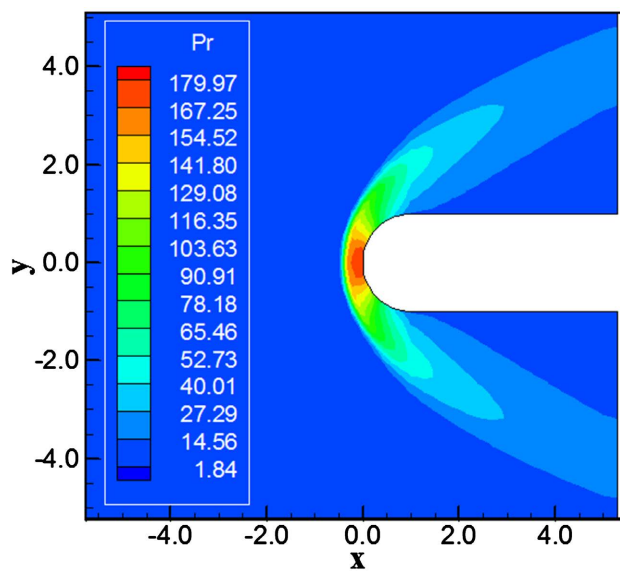
Figure 14. Pressure contours (LS-CGR-8th).
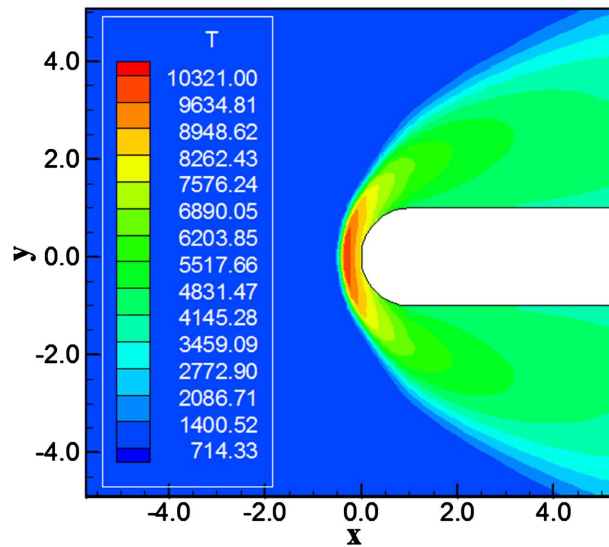
Figure 15. Temperature contours (LS-CGR-8th).
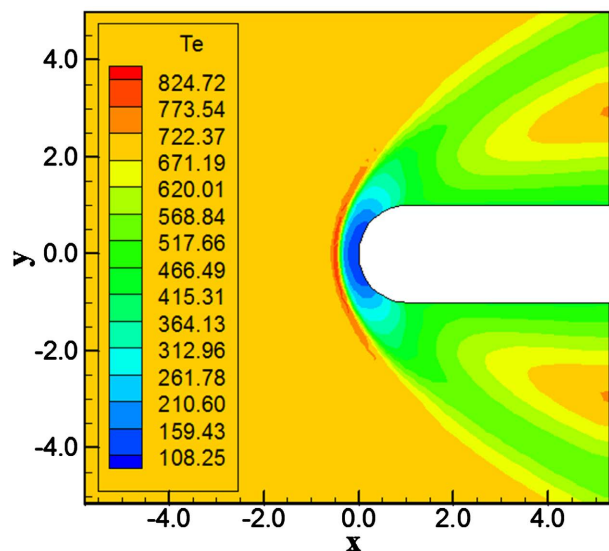
Figure 16. Electron temperature contours (LS-CGR-8th).

as well the temperature distributions along the body's wall obtained with the LS scheme using CGR Spectral method of 8th order of accuracy. The stagnation pressure is about 179.97 unites, whereas the stagnation translational/rotational temperature is estimated as 10,321.00 K. In Figure 16 the maximum electron temperature is obtained by the LS scheme with value 824.72 K. Some oscillations are perceptible in the electron temperature contours.

7.4. Double Ellipse

For the double ellipse problem, converged results were obtained with the CGR weighting function. It yields converged results for second, third, fourth, fifth, eighth and sixteenth orders of accuracy.

Figures 18-21 exhibit the pressure and temperature contours as well the
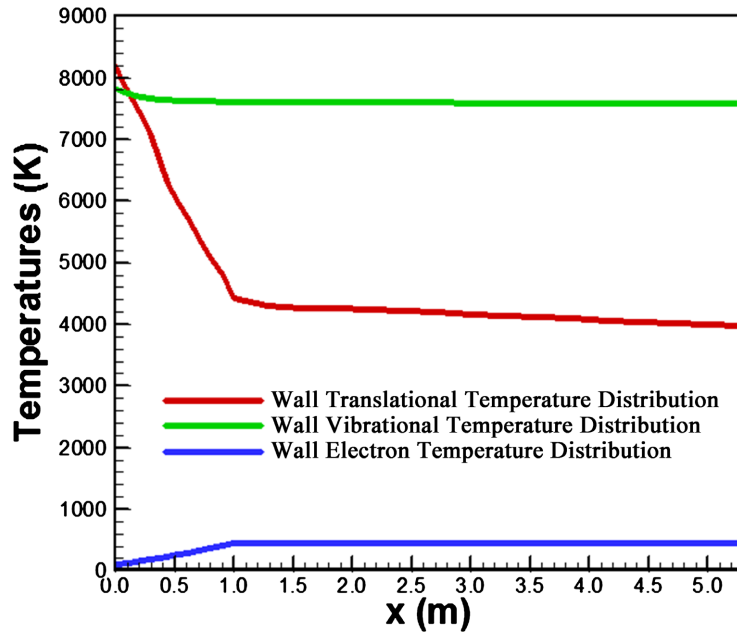
Figure 17. Wall temperature distributions (LS-CGR-8th).
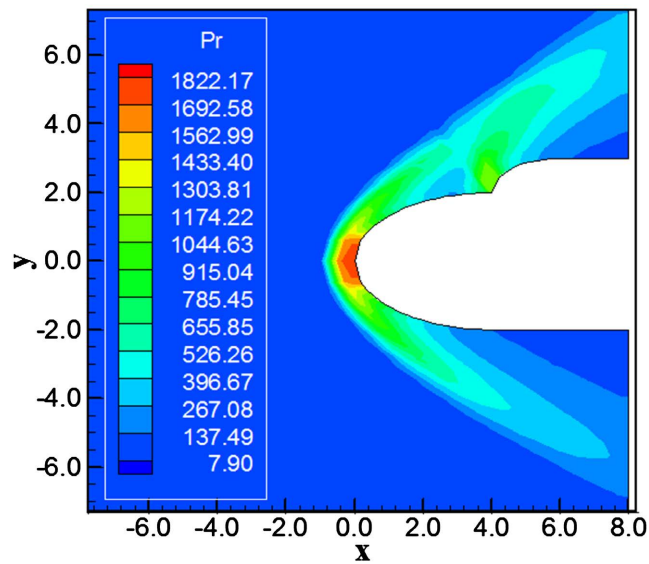
Figure 18. Pressure contours (LS-CGR-16th).

temperature distribution profiles along the body's wall obtained with the LS scheme as using the Spectral method of 16th order of accuracy, with CGR weighting function.

The maximum pressure is obtained at the body's nose with the value of 1822.17 unities, whereas the maximum temperature is obtained with the value of 11,025.30 K. The maximum electron temperature is obtained with the value of 302.40 K. The wall temperature profiles are shown at **Figure 21**. In this figure the vibrational temperature is quasi-constant and is unsymmetrical due to the asymmetry of the configuration. The electron profile has also a quasi-constant profile along the wall. The translational/rotational temperature profile reaches a minimum at
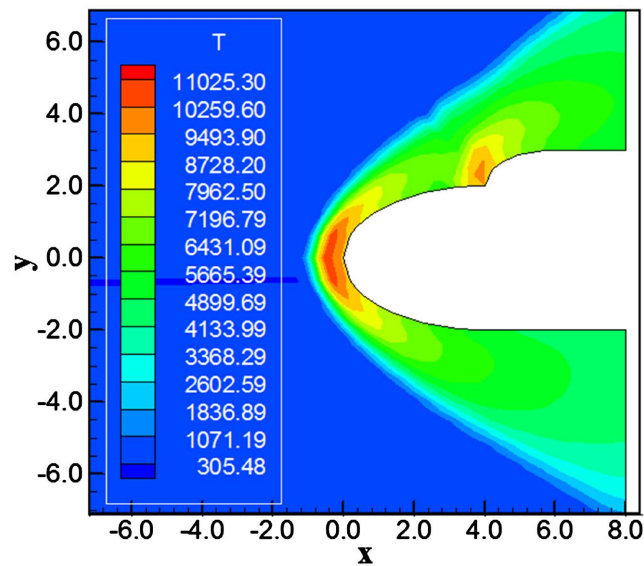
Figure 19. Temperature contours (LS-CGR-16th).
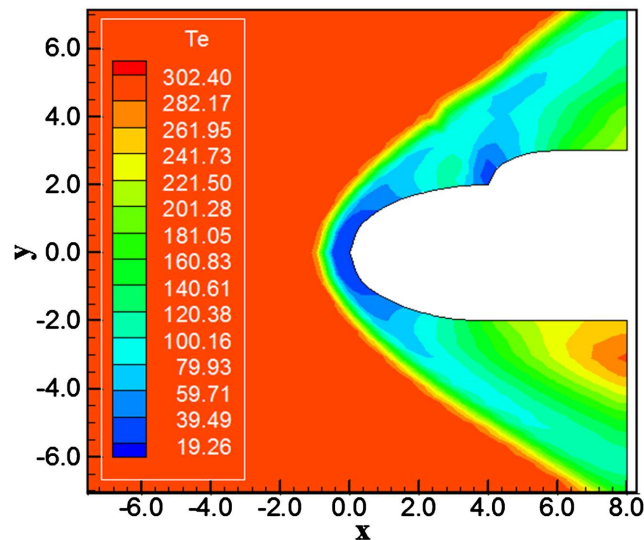
Figure 20. Electron temperature contours (LS-CGR-16th).

the body's end, close to 5000 K.

7.5. Error Analysis

In order to perform an error analysis, the present reactive results are compared to the perfect gas solutions. The stagnation pressure at the blunt body nose, circumference nose and reentry capsule nose were evaluated assuming the perfect gas formulation. Such parameter calculated at this way is not the best comparison, but in the absence of practical reactive results, this constitutes the best available solution. To calculate the stagnation pressure ahead of the blunt body, for example, [28] presents in its B Appendix values of the normal shock wave properties ahead of the configuration. The ratio pr_0/pr_∞ is estimated as function of the normal Mach number and the stagnation pressure pr_0 can be determined
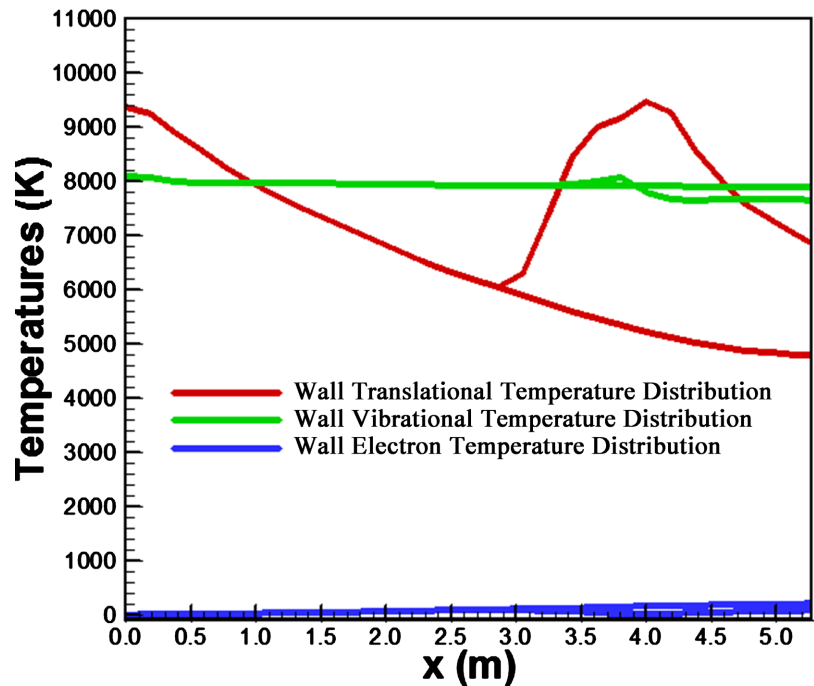
Figure 21. Wall temperature distributions (LS-CGR-16th).

from this parameter. The value of pr_∞ is determined by the following expression:

$$pr_\infty = \frac{pr_{initial}}{\rho_\infty a_\infty^2},\qquad(66)$$

where, for example, for the blunt body problem, $pr_{initial}$ = 687 N/m², ρ_∞ = 0.004 kg/m³ and a_∞ = 317.024 m/s. Considering these values, one concludes that pr_∞ = 1.709 (non-dimensional). Using the ratio obtained from [28], the stagnation pressure ahead of the configuration nose is estimated as 170.87 unities. Taking into account these calculations, it is possible to establish the following data disposed in Table 6.

Tables 7-11 compare the values of the stagnation pressure obtained from the simulations with these theoretical values and show the percentage errors. Table 7 has the circumference data, Table 8 has the reentry capsule data, and Table 9 has the inviscid blunt body data. Finally, Table 10 has the viscous blunt body data and Table 11 has the double ellipse data. These results are composed by all converged results obtained in this study, with the majority not exhibited in this article due to paper size.

As can be observed, the best solution to the circumference problem was obtained by the SW scheme using the CGR spectral method of second order, with the estimation error of the stagnation pressure of only 5.69%. To the reentry capsule problem, the best solution was again obtained with the SW scheme, addressing the minimum relative error of 0.11% in the estimative of the stagnation pressure. It was also obtained with the CGR spectral method of [6], in its fifth order of accuracy. To the third problem, the blunt body configuration, two error analysis were done: one for the inviscid case and the other for the viscous case.

Table 6. Values of theoretical stagnation pressure.

Problem	$M_{initial}$	pr_0/pr_∞	pr_∞	pr_0
Circumference	14.80	282.72	5.945	1680.77
Reentry Capsule	10.60	145.46	9.664	1405.73
Blunt Body	8.78	99.98	1.709	170.87
Double Ellipse	15.00	290.20	7.109	2063.03

Table 7. Values of stagnation pressure and respective errors (Circumference Problem).

Method	Order	Scheme	pr_0	Error
Spectral—CGR	2nd	SW	1585.09	5.69%
Spectral—CGR	3rd	SW	1443.08	14.14%
Spectral—CGR	4th	SW	1398.89	16.77%
Spectral—CGR	5th	SW	1355.69	19.34%
Spectral—CGR	8th	SW	1341.23	20.20%
Spectral—CGR	16th	SW	1287.19	23.42%

Table 8. Values of stagnation pressure and respective errors (Reentry Capsule Problem).

Method	Order	Scheme	pr_0	Error
Spectral—CGR	2nd	VL	1610.38	14.56%
Spectral—CGR	2nd	SW	1610.86	14.59%
Spectral—CGR	3rd	VL	1494.54	6.32%
Spectral—CGR	3rd	SW	1484.87	5.63%
Spectral—CGR	4th	VL	1458.01	3.72%
Spectral—CGR	4th	SW	1445.76	2.85%
Spectral—CGR	5th	VL	1422.67	1.21%
Spectral—CGR	5th	SW	1407.27	0.11%
Spectral—CGR	8th	VL	1358.72	3.34%
Spectral—CGR	8th	SW	1376.77	2.06%
Spectral—CGR	16th	VL	1333.41	5.14%
Spectral—CGR	16th	SW	1312.50	6.63%

For the inviscid case, the best value of the stagnation pressure was obtained by the VL scheme using the CGR spectral method in its second order of accuracy, with an error of 0.33%. On the other hand, for the viscous case, the best estimative of the stagnation pressure was obtained by the LS scheme using CGR and sixteenth order of accuracy, presenting an error of 2.69%. Finally, for the fourth problem, the double ellipse problem, the best solution in terms of stagnation pressure estimation was obtained by the LS scheme using the CGR spectral method

Table 9. Values of stagnation pressure and respective errors (Blunt Body Inviscid Problem).

Method	Order	Scheme	p_{r_0}	Error
Spectral—CGR	2nd	VL	170.31	0.33%
Spectral—CGR	2nd	LS	188.32	10.21%
Spectral—CGR	2nd	SW	160.88	5.85%
Spectral—CGR	3rd	VL	157.07	8.08%
Spectral—CGR	3rd	LS	178.41	4.41%
Spectral—CGR	3rd	SW	146.52	14.25%
Spectral—CGR	4th	VL	153.46	10.19%
Spectral—CGR	4th	LS	175.29	2.59%
Spectral—CGR	4th	SW	141.94	16.93%
Spectral—CGR	5th	VL	149.24	12.66%
Spectral—CGR	5th	LS	172.19	0.77%
Spectral—CGR	5th	SW	137.47	19.55%
Spectral—CGR	8th	VL	143.88	15.80%
Spectral—CGR	8th	LS	168.14	1.60%
Spectral—CGR	8th	SW	131.80	22.87%
Spectral—CGR	16th	VL	138.86	18.73%
Spectral—CGR	16th	LS	164.38	3.80%
Spectral—CGR	16th	SW	126.50	25.97%

Table 10. Values of stagnation pressure and respective errors (Blunt Body Viscous Problem).

Method	Order	Scheme	p_{r_0}	Error
Spectral—CGR	2nd	LS	206.32	20.75%
Spectral—CGR	3rd	VL	203.65	19.18%
Spectral—CGR	3rd	LS	192.33	12.56%
Spectral—CGR	3rd	SW	203.21	18.93%
Spectral—CGR	4th	VL	198.50	16.17%
Spectral—CGR	4th	LS	188.44	10.28%
Spectral—CGR	4th	SW	198.68	16.28%
Spectral—CGR	5th	VL	193.66	13.34%
Spectral—CGR	5th	LS	184.72	8.11%
Spectral—CGR	5th	SW	194.44	13.79%
Spectral—CGR	8th	VL	187.40	9.67%
Spectral—CGR	8th	LS	179.97	5.33%
Spectral—CGR	8th	SW	186.65	9.24%
Spectral—CGR	16th	VL	181.74	6.36%
Spectral—CGR	16th	LS	175.46	2.69%
Spectral—CGR	16th	SW	181.21	6.05%

Table 11. Values of stagnation pressure and respective errors (Double Ellipse Problem).

Method	Order	Scheme	pn_0	Error
Spectral—CGR	2nd	VL	2166.61	5.02%
Spectral—CGR	2nd	LS	2099.83	1.77%
Spectral—CGR	2nd	SW	2183.46	5.84%
Spectral—CGR	3rd	VL	2001.37	2.99%
Spectral—CGR	3rd	LS	1978.05	4.12%
Spectral—CGR	3rd	SW	1992.25	3.43%
Spectral—CGR	4th	VL	1952.03	5.38%
Spectral—CGR	4th	LS	1939.83	5.97%
Spectral—CGR	4th	SW	1934.12	6.25%
Spectral—CGR	5th	VL	1901.87	7.81%
Spectral—CGR	5th	LS	1902.05	7.80%
Spectral—CGR	5th	SW	1877.56	8.99%
Spectral—CGR	8th	VL	1840.69	10.78%
Spectral—CGR	8th	LS	1855.22	10.07%
Spectral—CGR	8th	SW	1807.75	12.37%
Spectral—CGR	16th	VL	1815.57	11.99%
Spectral—CGR	16th	LS	1822.17	11.68%
Spectral—CGR	16th	SW	1746.49	15.34%

in its second order accuracy, with an error of 1.77%.

7.6. Grid Convergence Index (GCI)

The discretization error ([29]) will be estimated using a method popular in the Computational Fluid Dynamics (CFD) community called the Grid Convergence Index (GCI), due to [30]. Two analyses are possible: constant grid refinement ratio and non-uniform grid refinement ratio. In the present study, the constant grid refinement ratio was considered and will be presented in this section. The property under analysis is the maximum pressure, stagnation pressure, of the blunt body problem, obtained by the [9] flux vector splitting scheme using the CGR spectral method of 2nd order.

Constant Grid Refinement Ratio. For the special case where the meshes are constructed with a constant grid refinement ratio, r, e.g. $r = h_2/h_1 = h_3/h_2 = $ constant where $h_1 < h_2 < h_3$, for a finite volume formulation, the convergence rate, p, can be estimated as

$$p = \frac{\left| \log_{10}\left(\frac{f_3 - f_2}{f_2 - f_1} \right) \right|}{\log_{10}(r)} . \tag{67}$$

where f_1, f_2 and f_3 are numerical values of the property under investigation for each mesh. Once the observed order-of-convergence is known, an estimate of the error between the fine grid solution and the unknown exact solution can be done. The relative error between the two finest grids is given by

$$e_{21} = \left| \frac{f_2 - f_1}{f_1} \right|.$$ (68)

The Grid Convergence Index (GCI) provides an estimate of the amount of discretization error in the finest grid solution relative to the converged numerical solution. Note the discretization error is with respect to the convergent numerical solution, as the exact solution is generally unknown. The GCI is given by

$$GCI_{21} = F_s \frac{e_{21}}{r_{21}^p - 1}.$$ (69)

where F_s is a "safety factor" multiplying the relative error term. The safety factor, $F_s = 1.25$, is based on experience applying GCI in many situations, [30]. The safety factor should be thought of as representing a 95% confidence bound on the estimated relative error. Example: say $f_1 = 5$ with a GCI = 2%, then the following statement can be made:

The converged numerical solution lies in the interval [4.90, 5.10], *i.e.* [f_1 (1 − GCI), f_1 (1 + GCI)], *with a* 95% *confidence level.*

Finally, based upon the two finest mesh solutions, and the estimate of the observed convergence rate, an extrapolation of the numerical solution is possible:

$$f_{21}^* = \frac{r_{21}^p f_1 - f_2}{r_{21}^p - 1}.$$ (70)

The extrapolation solution, f_{21}^*, provides a useful estimate of the converged solution, [29].

For the present work, it was chosen three meshes to observe the behavior of the maximum pressure in the simulations. The meshes are composed of 14,518 cells (123 × 120), 3658 cells (63 × 60), and 986 cells (35 × 30). The numerical values of the maximum pressure observed in the simulations were: $f_1 = 188.89$, $f_2 = 160.88$, and $f_3 = 118.94$. The ratio $r_{21} = h_2/h_1 = 2.0$ and the ratio $r_{32} = h_3/h_2 = 2.0$, where r is constant. Hence, the value of the convergence rate is calculated by

$$p = \frac{\left| \log_{10} \left(\frac{f_3 - f_2}{f_2 - f_1} \right) \right|}{\log_{10}(r)} = \frac{\left| \log_{10} \left(\frac{118.94 - 160.88}{160.88 - 188.89} \right) \right|}{\log_{10}(2.0)} = \frac{0.17532}{0.30103} = 0.58240.$$ (71)

The relative error e_{21} is calculated as

$$e_{21} = \left| \frac{f_2 - f_1}{f_1} \right| = \left| \frac{160.88 - 188.89}{188.89} \right| = 0.14829.$$ (72)

and GCI_{21} can be calculated as

$$GCI_{21} = F_s \frac{e_{21}}{r_{21}^p - 1} = 1.25 \times \frac{0.14829}{2.0^{0.58240} - 1} \quad \therefore GCI_{21} = 0.37231.$$ (73)

The interval of solution for this parameter is

$$S = \left[f_1 \left(1 - \text{GCI}_{21} \right), f_1 \left(1 + \text{GCI}_{21} \right) \right] = \left[118.56436, 259.21564 \right], \qquad (74)$$

with a 95% confidence level. Finally, the extrapolation solution is calculated by:

$$f_{21}^* = \frac{r_{21}^p f_1 - f_2}{r_{21}^p - 1} = \frac{2.0^{0.58240} \times 188.89 - 160.88}{2.0^{0.58240} - 1} = 245.21 . \qquad (75)$$

This value corresponds to the expected numerical solution to be obtained. This also suggests that the more realistic value to the stagnation pressure, taking into account the chemical effects, should be higher than 200.00 unities in place of 170.87 unities. The solution presented in this manuscript assumed the value f_2 = 160.88 and the error in relation to the extrapolation solution is 34.39%. However, it pertains to the 95% confidence level, which suggests that a more refined mesh is optional.

7.7. Three-Temperature Effect

The three-temperature effect can be seen in Table 12 and Table 13, where the values of the minimum errors committed by each scheme are compared with the present paper and the reference [31], which was an old work of the present author. Comparing the two tables, it is possible to highlight the better performance of the three-temperature model in relation to the two-temperature model of [31]. Of course, this comparison is not the best because such study should be accomplished with 4th order of accuracy by both works, for example. But as the 4th order study of [31] incorporated the best results for the inviscid case for each problem, so, the present results compare better than the old work. The unique loss of accuracy in relation to the old work (0.23%) was for the blunt body problem in its inviscid case (0.33%). All other comparisons exhibit the best performance of the three-temperature model, with maximum error of the order of

Table 12. Values of stagnation pressure and respective errors (Inviscid case).

Problem	Method	Order	Scheme	Error	Reference
Reentry Capsule	Spectral—CGR	4th	LS	5.06%	[31]
Reentry Capsule	Spectral—CGR	5th	SW	0.11%	This one
Blunt Body	Spectral—CGR	4th	VL	0.23%	[31]
Blunt Body	Spectral—CGR	2nd	VL	0.33%	This one
Double Ellipse	Spectral—CGR	4th	LS	2.71%	[31]
Double Ellipse	Spectral—CGR	2nd	LS	1.77%	This one

Table 13. Values of stagnation pressure and respective errors (Viscous case).

Problem	Method	Order	Scheme	Error	Reference
Blunt Body	Spectral—CGR	16th	LS	3.42%	[31]
Blunt Body	Spectral—CGR	16th	LS	2.69%	This one

2.69%. Finally, it is important to highlight better performance of the three-temperature model in the determination of the stagnation pressure for the studied configurations, than the two-temperature model.

In summary, the paper has presented results for the four studied cases and has compared them with literature theoretical results of [28]. The advantage of the present implementation is evident by the minimum errors found in each case in the present study and for the comparison of results with another reference [31], also of this author, that presented worse values for the stagnation pressure estimation in relation to this paper. The three-temperature model performance was highlighted in this section, emphasizing this one as more accurate them other two-temperature models. Particularly, the results of [31] were obtained with a computational code written in FORTRAN language and the present results with a code written in OBJECT PASCAL language. So, the performances are different and the realistic comparison between codes are evident, with better behavior for the later implementation with the proposed three-temperature model.

The advantages of the present formulation with a three-temperature model is highlighted by the good numerical results obtained in terms of percentage errors, with values close to 0.11% in the best case, and in comparison with other references as [31]. About the effectiveness of the proposed model, this can be observed that the implemented spectral method, used to high order analysis, has presented converged results for the majority of the studied cases, evidencing the appropriated formulation presented here. Moreover, the three algorithms have presented converged results, emphasizing the correct implementation and, as they are upwind and flux vector splitting schemes, don't requiring artificial dissipation to guarantee convergence, they are also cheaper than the flux difference splitting counterparts. The fact of not requiring artificial dissipation is a critical advantage of these schemes, eliminating the phase of user trial and error approaches to convergence and providing a solution with the appropriated level of dissipation.

8. Conclusions

In this work, a study involving the fully coupled Euler and Navier-Stokes reactive equations is performed. These equations, in conservative and finite volume contexts, employing structured spatial discretization, on a condition of thermochemical non-equilibrium, are analyzed. High-order studies are accomplished using the spectral method of Street *et al*. The high enthalpy hypersonic flows around a circumference, around a reentry capsule, along a blunt body, and along a double ellipse in two-dimensions are simulated. The Van Leer, Liou and Steffen Jr., and the Steger and Warming flux vector splitting algorithms are applied to execute the numerical experiments. The Euler backward integration method is employed to march the schemes in time. The convergence process is accelerated to steady state condition through a spatially variable time step procedure, which has proved effective gains in terms of computational acceleration (see

Maciel). The reactive simulations involve Earth atmosphere chemical model of seven species and eighteen reactions, based on the Blottner model. Three temperatures are used to accomplish the numerical comparisons.

The results have demonstrated that the Liou and Steffen Jr. and Steger and Warming schemes were the best in the estimative of the stagnation pressure ahead of the hypersonic geometries studied in this work. For the circumference problem, the best solution was obtained by the Steger and Warming scheme using the CGR spectral method of second order, with the estimation error of the stagnation pressure of only 5.69%. To the reentry capsule problem, the best solution was again obtained with the Steger and Warming scheme, addressing the minimum relative error of 0.11% in the estimative of the stagnation pressure. It was also obtained with the CGR spectral method of Street *et al.*, in its fifth order of accuracy. To the third problem, the blunt body configuration, two error analysis were done: one for the inviscid case and the other for the viscous case. For the inviscid case, the best value of the stagnation pressure was obtained by the Van Leer scheme using the CGR spectral method in its second order of accuracy, with an error of 0.33%. On the other hand, for the viscous case, the best estimative of the stagnation pressure was obtained by the Liou and Steffen Jr. scheme using CGR weighting function and sixteenth order of accuracy, presenting an error of 2.69%. Finally, for the fourth problem, the double ellipse problem, the best solution in terms of stagnation pressure estimation was obtained by the Liou and Steffen Jr. scheme using the CGR spectral method in its second order accuracy, with an error of 1.77%.

The main contribution of this work to the CFD community was the implementation of three-temperature model coupled with three flux vector splitting algorithms to the solution of reentry flow problems in 2D and the use of a spectral method to error analysis. With it, numerical tools are available to study thermochemical non-equilibrium flows in two-dimensions more realistically. The detailed source terms implemented to consider electron temperature and more realistic simulations were remarkable contributions from this work. Finally, this in house code was implemented in Object PASCAL language, with the use of Delphi software produced by Borland.

Conflicts of Interest

The author declares no conflicts of interest regarding the publication of this paper.

References

[1] Howe, J.T. (1985) Introductory Aerothermodynamics of Advanced Space Transportation Systems. *Journal of Spacecraft and Rockets*, **22**, 19-26. https://doi.org/10.2514/3.25705

[2] Madjarevic, D., Ruggeri, T. and Simic, S. (2014) Shock Structure and Temperature Overshoot in Macroscopic Multi-Temperature Model of Mixtures. *Physics of Fluids*, **26**, Article ID: 106102. https://doi.org/10.1063/1.4900517

[3] Cai, C. and Huang, X. (2011) A Kinetic BGK Scheme for Non-Equilibrium Gaseous Flow Computation. 20*th AIAA Computational Fluid Dynamics Conference*, Honolulu, 27-30 June 2011, AIAA Paper 2011-3543.

[4] Zhong, X., MacCormack, R.W. and Chapman, D.R. (1993) Stabilization of the Burnett Equations and Application to Hypersonic Flows. *AIAA Journal*, **31**, 1036-1043. https://doi.org/10.2514/3.11726

[5] Gottlieb, D. and Orszag, S. (1987) Numerical Analysis of Spectral Methods: Theory and Applications. Society for Industrial and Applied Mathematics, Philadelphia. https://doi.org/10.1137/1.9781611970425

[6] Streett, C.L., Zang, T.A. and Hussaini, M.Y. (1984) Spectral Methods for Solution of the Boundary-Layer Equations. AIAA Paper 84-0170. https://doi.org/10.2514/6.1984-170

[7] Van Leer, B. (1982) Flux-Vector Splitting for the Euler Equations. 8th International Conference on Numerical Methods in Fluid Dynamics, Vol. 170, Aachen, 28 June-2 July 1982, 507-512. https://doi.org/10.1007/3-540-11948-5_66

[8] Liou, M. and Steffen Jr., C.J. (1993) A New Flux Splitting Scheme. *Journal of Computational Physics*, **107**, 23-39. https://doi.org/10.1006/jcph.1993.1122

[9] Steger, J.L. and Warming, R.F. (1981) Flux Vector Splitting of the Inviscid Gasdynamic Equations with Application to Finite-Difference Methods. *Journal of Computational Physics*, **40**, 263-293. https://doi.org/10.1016/0021-9991(81)90210-2

[10] Maciel, E.S.G. (2015) Simulations in 2D and 3D Applying Unstructured Algorithms, Euler and Navier-Stokes Equations—Perfect Gas Formulation. Lambert Academic Publishing (LAP), Saarbrücken, Ch. 1, 26-47.

[11] Maciel, E.S.G. (2015) Simulations in 2D and 3D Applying Unstructured Algorithms, Euler and Navier-Stokes Equations—Perfect Gas Formulation. Lambert Academic Publishing (LAP), Saarbrücken, Ch. 6, 160-181.

[12] Blottner, F.G. (1969) Viscous Shock Layer at the Stagnation Point with Nonequilibrium Air Chemistry. *AIAA Journal*, **7**, 2281-2288. https://doi.org/10.2514/3.5528

[13] Maciel, E.S.G. (2021) A Spectral Method Applied to Re-entry Flow Problems. Volume 2—Chemical and Thermochemical Non-Equilibrium Applications to Reentry Flows. Lambert Academic Publishing (LAP), Republic of Moldova.

[14] Davis, P.A. and Rabinowitz, P. (1967) Numerical Integration. Blaisdell Publishing Co., Waltham.

[15] Canuto, C., Hussaini, M.Y., Quarteroni, A. and Zang, T.A. (2007) Spectral Methods: Evolution to Complex Geometries and Applications to Fluid Dynamics. Scientific Computation Springer, Berlin, Heidelberg. https://doi.org/10.1007/978-3-540-30728-0

[16] Prabhu, R.K. (1994) An Implementation of a Chemical and Thermal Nonequilibrium Flow Solver on Unstructured Meshes and Application to Blunt Bodies. National Aeronautics and Space Administration, Washington DC, NASA CR-194967.

[17] Saxena, S.K. and Nair, M.T. (2005) An Improved Roe Scheme for Real Gas Flow. 43*rd AIAA Aerospace Sciences Meeting and Exhibit*, Reno, 10-13 January 2005, AIAA Paper 2005-0587. https://doi.org/10.2514/6.2005-587

[18] Maciel, E.S. G. (2015) Hypersonic Reactive Flow Simulations in Two-Dimensions, Chemical and Thermochemical Non-Equilibrium Conditions. Lambert Academic Publishing (LAP), Saarbrücken, Ch. 5, 333-406.

[19] Maciel, E.S.G. (2015) Hypersonic Reactive Flow Simulations in Two-Dimensions, Chemical and Thermochemical Non-Equilibrium Conditions. Lambert Academic

Publishing (LAP), Saarbrücken, Ch. 6, 407-490.

[20] Candler, G.V. and MacCormack, R.W. (1991) Computation of Weakly Ionized Hypersonic Flows in Thermochemical Nonequilibrium. *Journal of Thermophysics and Heat Transfer*, **5**, 266-273. https://doi.org/10.2514/3.260

[21] Lee, J.H. (1985) Basic Governing Equations for the Flight Regimes of Aeroassisted Orbital Transfer Vehicles. Thermal Design of Aeroassisted Transfer Vehicles. *Progress in Astronautics and Aeronautics*, **96**, 3-53. https://doi.org/10.2514/5.9781600865718.0003.0053

[22] Kim, M., Gülhan, A. and Boyd, I.D. (2011) Modeling of Electron Temperature in Hypersonic Flows. 49*th AIAA Aerospace Sciences Meeting including the New Horizons Forum and Aerospace Exposition*, Orlando, 4-7 January 2011, AIAA Paper 2011-1028. https://doi.org/10.2514/6.2011-1028

[23] Ait-Ali-Yahia, D. and Habashi, W.G. (1997) Finite Element Adaptive Method for Hypersonic Thermochemical Nonequilibrium Flows. *AIAA Journal*, **35**, 1294-1302. https://doi.org/10.2514/2.260

[24] Radespiel, R. and Kroll, N. (1995) Accurate Flux Vector Splitting for Shocks and Shear Layers. *Journal of Computational Physics*, **121**, 66-78. https://doi.org/10.1006/jcph.1995.1179

[25] Long, L.N., Khan, M.M.S and Sharp, H.T. (1991) Massively Parallel Three-Dimensional Euler/Navier-Stokes Method. *AIAA Journal*, **29**, 657-666. https://doi.org/10.2514/3.10635

[26] Vincenti, W.G. and Kruger Jr., C.H. (1965) Introduction to Physical Gas Dynamics. John Wiley & Sons, New York, London, Sidney.

[27] Fox, R.W. and McDonald, A.T. (1988) Introdução à Mecânica dos Fluidos. Guanabara Editor, Rio de Janeiro.

[28] Anderson Jr., J.D. (2010) Fundamentals of Aerodynamics. 5th Edition, McGraw-Hill, Inc., New York.

[29] Schwer, L.E. (2008) Is Your Mesh Refined Enough? Estimating Discretization Error using GCI. LS-DYNA Anwenderforum, Bamberg.

[30] Roache, P.J. (1994) Perspective: A Method for Uniform Reporting of Grid Refinement Studies. *ASME Journal of Fluids Engineering*, **116**, 405-413. https://doi.org/10.1115/1.2910291

[31] Maciel, E.S.G. (2017) Spectral Method Applied to Thermochemical Non-Equilibrium Reentry Flows in 2D: Seven Species—High Order Analysis. *Journal of Scientific and Engineering Research*, **4**, 302-339.